Mechanically and Chemically Robust Sandwich-Structured C@Si@C Nanotube Array Li-Ion Battery Anodes

Jinyun Liu,[†,∥] Nan Li,[‡] Matthew D. Goodman,[†] Hui Gang Zhang,[†] Eric S. Epstein,[†] Bo Huang,[†] Zeng Pan,[†] Jinwoo Kim,[†] Jun Hee Choi,[#] Xingjiu Huang,[∥] Jinhuai Liu,[∥] K. Jimmy Hsia,[‡,§] Shen J. Dillon,[†] and Paul V. Braun*[,†,‡,§,⊥]

[†]Department of Materials Science and Engineering, [‡]Department of Mechanical Sciences and Engineering, [§]Frederick Seitz Materials Research Laboratory, [⊥]Beckman Institute for Advanced Science and Technology, University of Illinois at Urbana—Champaign, Urbana, Illinois 61801, United States, [∥]Research Center for Biomimetic Functional Materials and Sensing Devices, Institute of Intelligent Machines, Chinese Academy of Sciences, Hefei, Anhui 230031, China, and [#]Samsung Advanced Institute of Technology, Samsung Electronics, Suwon 443-803, South Korea

ABSTRACT Stability and high energy densities are essential qualities for emerging battery electrodes. Because of its high specific capacity, silicon has been considered a promising anode candidate. However, the several-fold volume changes during lithiation and delithiation leads to fractures and continuous formation of an unstable solid-electrolyte interphase (SEI) layer, resulting in rapid capacity decay. Here, we present a carbon—silicon—carbon (C@Si@C) nanotube sandwich structure that addresses the mechanical and chemical stability issues commonly associated with Si anodes. The C@Si@C nanotube array exhibits a capacity of ~2200 mAh g^{-1} (~750 mAh cm^{-3}), which significantly exceeds that of a commercial graphite anode, and a nearly constant Coulombic efficiency of ~98% over 60 cycles. In addition, the C@Si@C nanotube array gives much better capacity and structure stability compared to the Si nanotubes without carbon coatings, the ZnO@C@Si@C nanorods, a Si thin film on Ni foam, and C@Si and Si@C nanotubes. *In situ* SEM during cycling shows that the tubes expand both inward and outward upon lithiation, as well as elongate, and then revert back to their initial size and shape after delithiation, suggesting stability during volume changes. The mechanical modeling indicates the overall plastic strain in a nanotube is much less than in a nanorod, which may significantly reduce low-cycle fatigue. The sandwich-structured nanotube design is quite general, and may serve as a guide for many emerging anode and cathode systems.

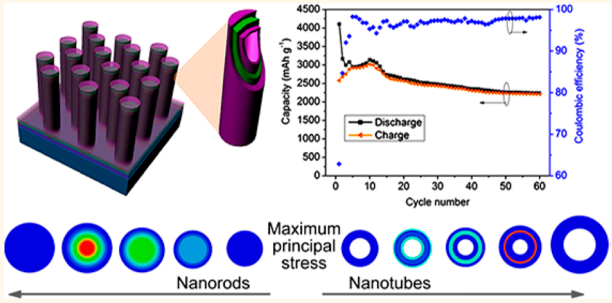

KEYWORDS: Li-ion battery · nanotube · silicon anode · capacity · plastic strain

Many applications require batteries with greater than currently available energy densities,[1−3] which has motivated numerous research efforts[4,5] including investigations on high energy density anode and cathode materials, and engineered electrode structures which maximize capacity utilization and rate performance.[6−9] Si has attracted broad attention as an anode material because of its high theoretical capacity of ~4200 mAh g^{-1}, which is about 10 times that of carbonaceous anodes.[10,11] However, Si expands ~300% during lithiation and subsequently contracts during delithiation, which leads to fracture, loss of contact between the active material and the current collector, and continuous formation of a solid-electrolyte interphase (SEI) layer.[12−14] SEI stabilization efforts have included carbon, oxide and polymer coatings.[15−17] Carbon coatings are attractive because they concurrently provide a conductive pathway within the electrode and form a barrier layer between the electrolyte and the Si.[18−20] For example, Cui *et al.* reported a Si/C hybrid inspired by a pomegranate structure in which Si nanoparticles are encapsulated in a larger carbon sphere, leaving a void that provides space for the volume expansion of the Si upon lithiation.[21] The carbon isolates the Si nanoparticles from the electrolyte, limiting SEI formation on the Si.

Here we fabricate, electrochemically cycle, and model the mechanics of a carbon-coated

* Address correspondence to pbraun@illinois.edu.

Received for review December 9, 2014 and accepted January 31, 2015.

Published online January 31, 2015
10.1021/nn507003z

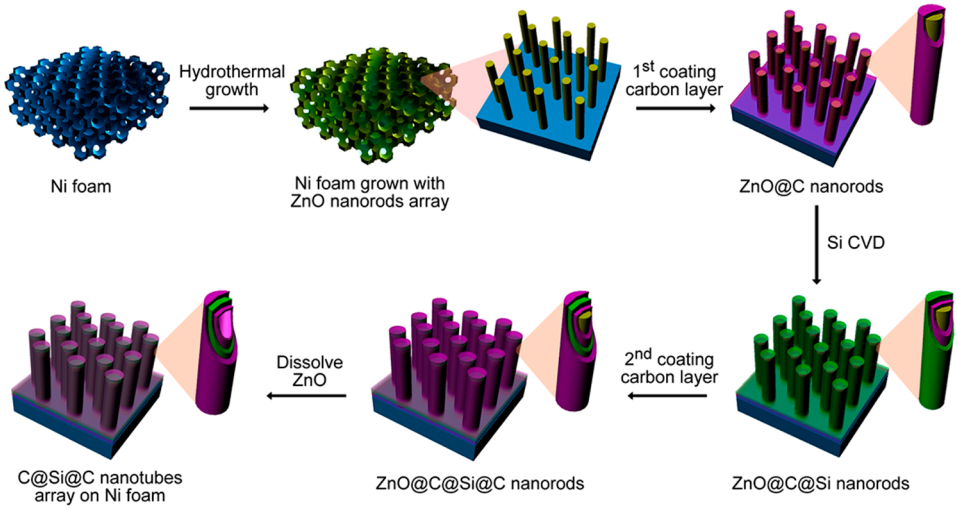

Figure 1. Schematic illustrating the fabrication of the 3D Ni foam supported sandwich-structured C@Si@C nanotube array.

tubular Si architecture designed to minimize the mechanical plastic strain associated with cycling and maintain a stable SEI. We show, relative to a solid rod, for example, the lithiated Si nanowires simulated by Zhang *et al.*,[22,23] that the plastic strain upon lithiation of a silicon tube is significantly less than that of a rod. A tubular architecture presents the possibility of a high energy density through the efficient packing of tubes, and carbon-coated tubes provide an efficient pathway for current collection, assuming the tubes are connected to a current collector, as is the case here. By growing the tubes on an electrically conductive 3D scaffold, thick electrodes with high energy densities can be fabricated. Specifically the electrode consists of sandwich-structured nanotubes arrayed on an electrically conductive Ni foam. The Si nanotubes are closed on one end, and are coated, both inside and outside, with a carbon layer (Figure 1). The electrode exhibits a gravimetric capacity of 2246 mAh g^{-1} (Si basis) and 200 mAh g^{-1} (electrode basis), and a volumetric capacity of 767 mAh cm^{-3}, which significantly exceeds that of a commercial graphite anode (~300 mAh cm^{-3}).[24] While the theoretical volumetric capacity of carbon is 830 mAh cm^{-3}, this does not include the current collector, binder, porosity, *etc*. The capacity fade of the structure is about 9.6% between the 20th and 60th cycle, and the Coulombic efficiency is about 98% over most C-rates.

RESULTS AND DISCUSSION

Fabrication of Sandwich-Structured C@Si@C Nanotube Electrode. A dense array of nearly uniform ~50 nm diameter, 500 nm long ZnO nanorods (Figure 2a and Figure S1a, Supporting Information) were hydrothermally grown onto a Ni foam (Figure S1b). The ZnO nanorods are then coated with 3−5 nm of carbon (Figure 2b), which in the final structure is the internal layer of the sandwich-structured nanotubes, by polymerizing a thin layer of furfuryl alcohol on the surface of ZnO nanorods (Figure S1c,d) followed by carbonization in Ar at 500 °C for 3 h. SEM images of the ZnO@C nanorod array are presented in Figure S1e,f. Twenty nanometers of Si was then deposited on the surface of the ZnO@C nanorods *via* static CVD (Figure 2c and Figure S1g,h), followed by the formation of a second 3−5 nm thick carbon layer, also by carbonization of a polymerized furfuryl alcohol layer (Figure 2d and Figure S1i,j). Finally, the ZnO nanorods were etched with dilute acetic acid, yielding the final C@Si@C nanotube structure.

Structural Characterization. X-ray diffraction (XRD) (Figure S2a) and energy dispersive X-ray (EDX) spectrometry (Figure S2b) confirm the crystalline nature of the hexagonal ZnO nanorods and presence of the Si coating, respectively. A cross-section of the layer-by-layer structure can be observed in a focused ion beam (FIB) milled sample (Figure S3). After etching the ZnO core, the sandwich nanotube structure can be visualized *via* SEM and TEM (Figure 2e,f). In Figure 1f, both the Si layer and the carbon layers can be observed. The sample composition and the complete removal of the ZnO core were confirmed by elemental mapping, EDX, and XRD (Figure S4).

Electrochemical Properties of the Sandwich-Structured C@Si@C Nanotube Array Anodes. The galvanostatic charge and discharge performance at 0.07 C (1 C corresponds to complete charge or discharge of theoretical capacity in 1 h) for 60 cycles is shown in Figure 3a. There is a long flat plateau during the first discharge (lithiation) consistent with previous reports on Si-based electrodes,[25,26] which can be assigned to the reaction between Si and Li-ion to form amorphous Li_xSi.[27] The electrode shows first cycle discharge and charge capacities of 4130 and 2545 mAh g^{-1} (Si basis), respectively giving an initial Coulombic efficiency of 61.6% (Figure 3b). For the second cycle, the Coulombic efficiency is

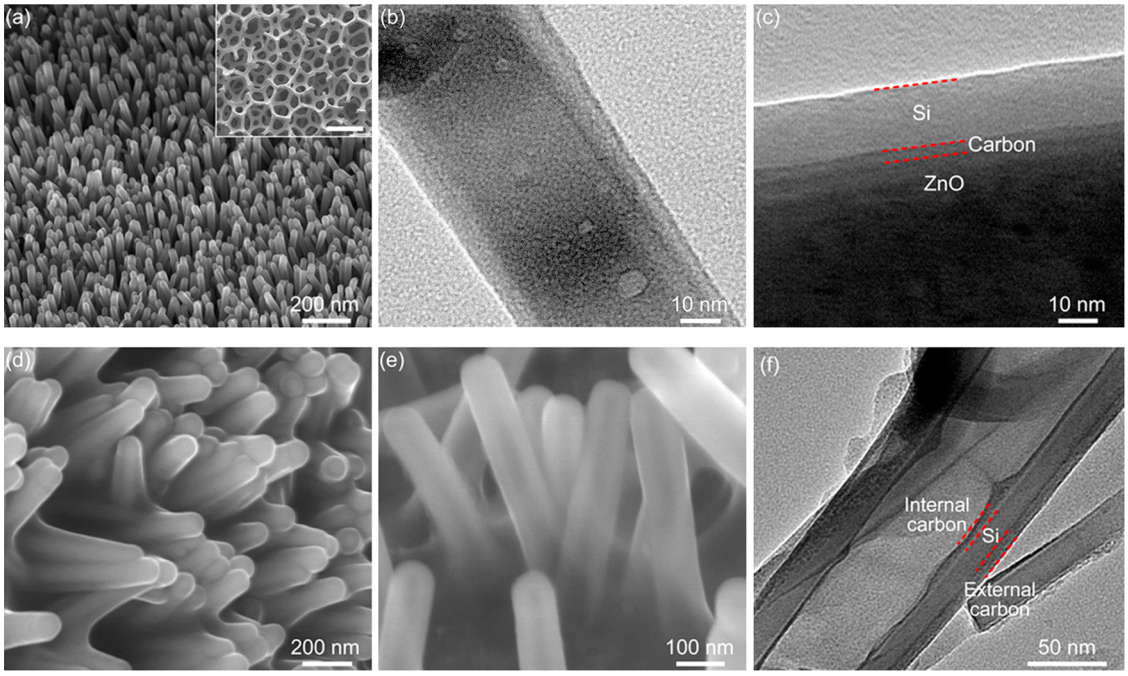

Figure 2. (a) SEM image of the ZnO nanorods grown on the Ni foam. The inset is a low-magnification SEM image of the ZnO nanorod array coated Ni foam (scale bar: 200 μm). (b) TEM image of a single carbon-coated ZnO nanorod after carbonization of carbon precursor-coated ZnO nanorods. (c) TEM image of a ZnO@C@Si nanorod. (d) SEM image of the ZnO@C@Si@C nanorod array. (e) SEM image of the C@Si@C nanotube array after etching the ZnO core. (f) TEM image of a C@Si@C nanotube.

85.1%, the discharge and charge capacities are 3181 and 2707 mAh g^{-1}, respectively. Over the first 10 cycles, the charge capacity gradually increases up to about 3006 mAh g^{-1}; the capacity increase with cycling for Si has previously been ascribed to the activation of Si.[28,29] After about 15 cycles, the cycling becomes stable, with a typical discharge capacity of 2246 mAh g^{-1}, charge capacity of 2208 mAh g^{-1}, and Coulombic efficiency of ~98.3%, which is considerably better than some previous reports,[30−33] although not as good as Cui's results.[21] The capacity then fades slowly over the following cycles, perhaps due to the choice of $LiClO_4$ in EC-DMC as the electrolyte. It was recently reported lithium hexafluorophosphate and fluorinated ethylene carbonate provide more stable cycling,[34] and such a system will be considered for future work. The initially very porous 3D electrode can be compressed from ~1000 to 150 μm thick without structural and electrochemical performance degradation (Figures S5 and S6), yielding an electrode volumetric capacity of 767 mAh cm^{-3}.

The cyclic voltammetry (CV) curves of the C@Si@C nanotube array at a scan rate of 0.1 mV s^{-1} over the range of 0.0 to 2.0 V are shown in Figure 3c and Figure S7. Reduction peaks around 0.04 and 0.19 V can be found in the cathodic branch of the curves, which can be attributed to the lithiation of Si to form Li_xSi alloys.[35,36] Starting from the second cycle, the weak cathodic peaks located round 0.5 V can be observed. No obvious oxidation peaks indicative of SEI formation are observed in the anodic sweep.[37] The anodic peaks at about 0.33 and 0.51 V overlap slightly, and can be assigned to reversible reactions between Li-ion and Si and probably correspond to the cathodic peaks around 0.04 and 0.19 V.[38] As seen in the inset in Figure 3c, the intensity of each peak increases with cycling, indicating the activation of more Si with Li during the charge/discharge process, in good agreement with the galvanostatic data.

Figure 3d shows the rate performance of the 3D electrodes (galvanostatic cycling curves are shown in Figure S8). All electrodes were precycled *ca.* 15 times at 0.06 C before C-rate measurements. Both charge and discharge capacities decrease as the C-rate increases; however, the Coulombic efficiency stays around 96−99%, indicating a stable electron transfer performance at all current densities, The electrode retains discharge and charge capacities of about 1235 and 1223 mAh g^{-1} even at a rate of 2 C. When the C-rate was returned to 0.05 C, the capacities recovered, and the Coulombic efficiency remained greater than 98%.

Control Architectures. To determine the origin of the electrochemical properties of the C@Si@C nanotube array structures, a series of related structures were fabricated including carbon-layer free Si nanotubes (Figure 4a, and Figure S9a,b), formed by growing Si directly on the ZnO nanorods followed by ZnO etching, ZnO@C@Si@C nanorods (Figure 4b, and Figure S9c,d), and a Si thin film grown directly on the Ni foam (Figure 4c). The electrochemical properties including discharge and charge capacities, and the corresponding

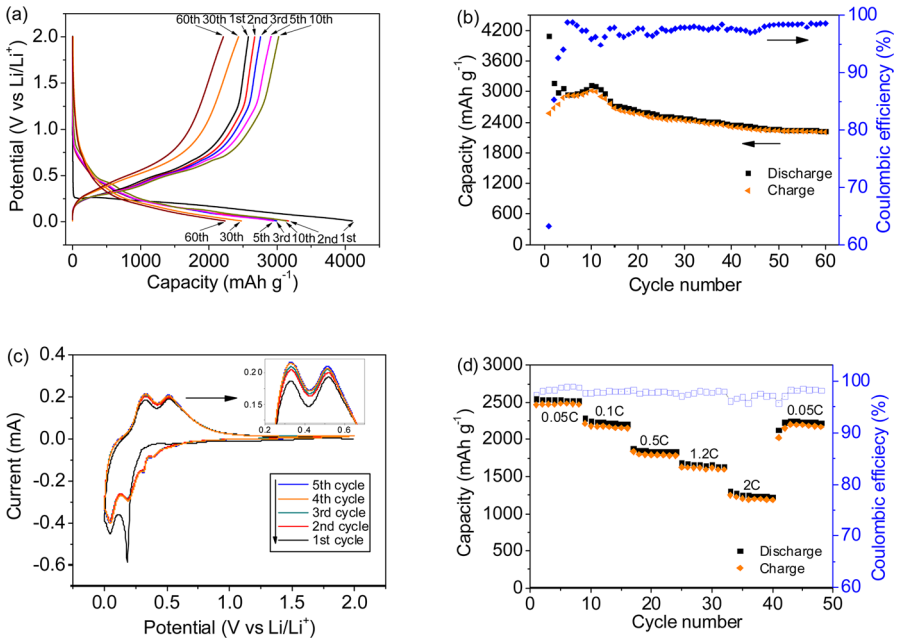

Figure 3. (a) Galvanostatic charge/discharge cycles at a rate of 0.07 C. (b) Specific capacity and Coulombic efficiency over 60 cycles. (c) The first five CV curves over the potential range of 0.0 to 2.0 V *versus* Li/Li^+ at a scan rate of 0.1 mV s^{-1}. (d) The C-rate performance of the electrode from 0.05 to 2 C.

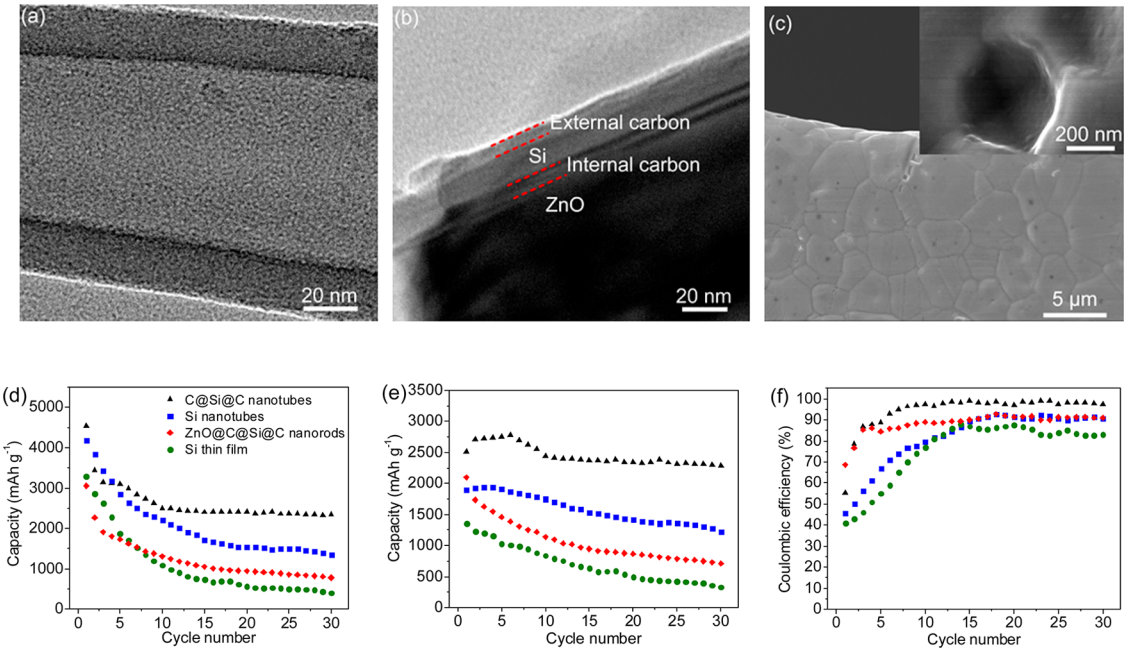

Figure 4. TEM images of (a) the Si nanotube and (b) the ZnO@C@Si@C nanorod. (c) SEM image of the Si thin film deposited on a strut of the Ni foam. The inset is a high-magnification image. (d) Discharge capacity, (e) charge capacity and (f) Coulombic efficiency of different structures at 0.08 C over 30 cycles.

Coulombic efficiency of these three electrodes, as well as the C@Si@C nanotube array at a rate of 0.08 C are shown in Figure 4d–f (galvanostatic cycling curves are shown in Figure S10). The discharge capacity of the Si nanotubes shows a pronounced decay to ~1800 mAh g^{-1} after 15 cycles, and after 15 cycles, the Si thin film shows a decay to below 1000 mAh g^{-1}. Both the Si nanotubes and the Si thin film show low Coulombic efficiencies, probably due to continuous SEI formation, which agrees with the thick SEI layer that can be observed in the SEM images after cycling (Figure S11a–d). The capacity of the ZnO@C@Si@C nanorods also decays rapidly, and obvious cracks after cycling are observed (Figure S11e,f). The solid core requires all volume expansion during lithiation to be outward, which is probably the origin of the cracks. C@Si (Figure S12a–c) and Si@C nanotubes (Figure S12d–f) were also fabricated and compared with the sandwich-structured nanotubes. These structures

give high discharge capacities (in particular the Si@C nanotubes) in the initial cycles (Figure S13); however, they both show obvious capacity decays to below 2000 mAh g^{-1} after 30 cycles.

We hypothesize the electrochemical performance of the C@Si@C nanotube array is superior to the other designs for the following reasons. The electrode design presented here consists of closed-end (Figure 2e) Si nanotubes sandwiched between two carbon layers. The external carbon layer appears to assist in formation of a stable SEI as can be noted by comparing Figure S14, where the carbon layer is present, and only a thin SEI forms, and Figure S11a–d, where no carbon is present, and a thick SEI forms. It is possible the carbon surface chemistry is playing a role due in SEI formation. Previous reports,[34,39,40] have found that the surface functionalities present on carbon depend on the fabrication processes and the SEI performance is a function of the surface chemistry.[41,42] To limit formation of SiO_2 and SiC, known to form at 900 °C when Si and carbon are both present, and known to prevents efficient lithitation-delithiation,[39] a heat treatment temperature of 500 °C was employed to pyrolyze furfuryl alcohol, and at this low of a temperature, there are almost certainly a diversity of surface chemical functionalities on the carbon layer. The internal carbon layer appears to play a significant role in providing a continuous conductive pathway for electron transfer, and may also limit SEI formation as noted by the significant reduction in capacity fade for a sandwich structure *vs* a structure with the carbon layer only on the outside. During lithiation–delithiation, the morphology of nanotube changes reversibly, retaining a stable tubular structure, as shown through the *in situ* SEM observations described below. It also should be noted that the acetic acid, which is used to etch the ZnO nanorods, presumably reaches the nanorods through pinholes or cracks in the Si tube; however, as SEI is not observed inside the C@Si@C nanotubes after cycling, it appears electrolyte may not substantially enter the tubes, perhaps because the pinholes become clogged by a thin SEI layer. The combination of the nanotube structure and the open structure of the 3D porous Ni scaffold accommodate the volume change of Si during lithiation–delithiation.

The improved electrochemical performance of the C@Si@C nanotube array sandwich structure relative to the Si nanotubes, the ZnO@C@Si@C nanorods, a Si thin film on Ni foam, and C@Si and Si@C nanotubes indicates the importance of each structural element of the nanotube array electrode. Impedance spectroscopy (EIS, Figure S15) indicates a stable surface chemistry and consistent Li ion diffusion kinetics for the C@Si@C nanotube array sandwich structure. In addition, the presented electrode is also designed to concurrently mitigate the effects of the volume changes of the Si while maintaining good ionic and electrical conductivities through the structure. The high surface area of the foam, results in a high density of ZnO nanorods, which leads to a high volume density of Si in the final structure. Because of the nanorod structure, substantially more Si is present in the final structure than if the Si was simply grown on the Ni foam. To increase both the gravimetric and volumetric capacity, structurally optimized 3D scaffolds, formed perhaps from lower density metals may be required; however, even without such efforts, this design already provides an volumetric capacity significantly greater than a commercial carbon-based anode.

***In Situ* Observations.** The lithiation and delithiation of a nanotube was observed *in situ* using a design which did not place external mechanical constraints on the tubes (the tubes are freely lying on a substrate). Even though the lithium diffusion pathways in the *in situ* studies are different than in an electrolyte flooded system, we suspect lithium surface diffusion on the surface of the nanotubes is fast enough that lithiation of the nanotubes is still homogeneous in the *in situ* experiments. Evidence for this is that the nanotubes do not appear to bend during lithiation in the *in situ* experiments, which would be the case if one side of the nanotubes lithiated first.

For *in situ* observations larger diameter C@Si@Cnanotubes were fabricated by starting with ~800 nm diameter ZnO rods; all subsequent fabrication steps were the same as for the standard electrode (larger rods were necessary to provide sufficient resolution during imaging). To keep the ratio of the thickness of the silicon to the diameter of the rods similar to the standard electrode, a thicker Si layer was grown (Figure S16). The volume changes with cycling can be observed in Figure 5a–c. There is an expansion during lithiation, and contraction during delithiation (video is shown as Movie S1). During lithiation, the tube exhibits both inward and outward expansion, along with elongation, and no obvious cracking was observed. The ratio of expansion and elongation is constant between the first and second lithiation (Figure S17 and Table S1), indicating the strain is reversible during lithiation–delithiation.

Mechanics Evaluation. The large volume changes during cycling lead to significant stresses in both lithiated and unlithiated Si.[43,44] The stress build-up is the results of two effects, external constraints (*e.g.*, the substrate) that prevent the lithiated Si from expanding freely, and the deformation mismatch between lithiated and unlithiated regions. Because lithiated Si is ductile, once the von Mises stress in the lithiated Si exceeds its yield strength,[45] plastic deformation begins. After yield, plastic strain can increase until it reaches the ultimate strain, at which point fracture occurs. If a material is stressed repetitively above the yield stress, but not strained to the ultimate strain, plastic deformation will still accumulate and eventually lead to fracture

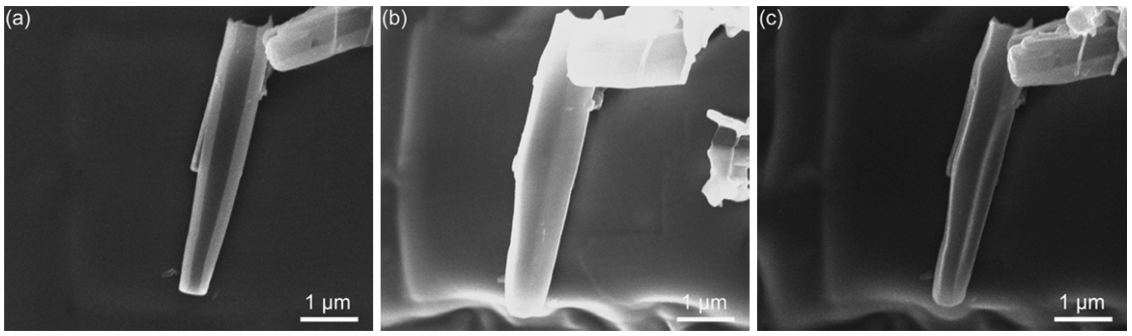

Figure 5. *In situ* observations: SEM images of a C@Si@C nanotube (a) as fabricated, (b) after discharge (lithiation), and (c) after charge (delithiation).

(low cycle fatigue). The greater the plastic strain in each cycle, the earlier the material will fail, thus the motivation for architectures which reduce the plastic strain for a given degree of lithiation.

The stress distributions and plastic strain in both the silicon nanotubes used in electrochemical measurements and the larger tubes used for the *in situ* SEM studies are studied here *via* finite element analysis (FEA) using ABAQUS,[46] and compared with Si nanorods with the same Si cross-sectional area. In the FEA, we assume that an atomically sharp reaction front migrates through Si nanowires during lithiation,[22,23] forming a sharp boundary between Li-poor and Li-rich phases. The reaction rate is considered to be constant and uniform ignoring the crystallographic orientation dependence,[47,48] leading to constant migration velocity (the Si used here is amorphous). We assume that the rate of lithiation is the same on the inside and outside walls of the tubes. The coefficient of linear expansion upon lithiation is chosen to be 60% to match the 300% volume expansion.[23] Young's moduli and Poisson's ratios of silicon and lithiated silicon are chosen to be 80 and 15 GPa, and 0.22 and 0.17, respectively.[12] The lithiated Si is considered to obey elastic-perfectly plastic constitutive law with a yielding stress of 0.5 GPa.[45]

Two stress components in the Si nanotubes and nanorods were evaluated as lithiation progresses: the maximum principal stress, which is responsible for crack initiation and propagation; and the von Mises stress, which drives plastic deformation. The magnitudes of the stresses in nanotubes and nanorods were compared to identify possible failure mechanisms. Figures 6 and 7 show the highest maximum principal stress as a function of the thickness ratio, and the contours of the maximum principal stress in the nanotubes and nanorods (contours of the von Mises stress shown in Figure S18), respectively. For both the nanotubes and the nanorods, the thickness ratio is defined as silicon equivalent thickness of the lithiated region divided by that of the original total thickness of the silicon. For the nanorods, the original total thickness of the silicon is the original nanorod radius, and for the

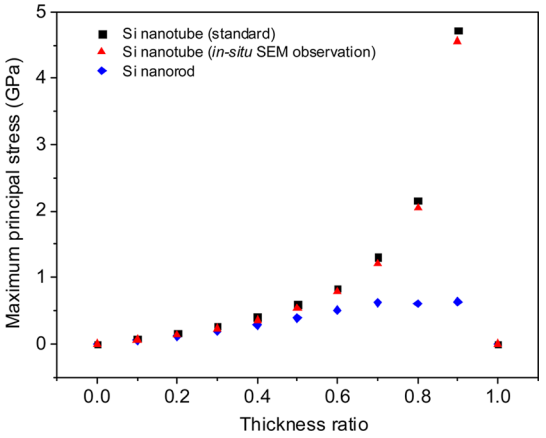

Figure 6. Maximum principal stress in the silicon nanotubes and the nanorods as a function of lithiation (expressed as the thickness ratio as defined in the text). The Si nanotube (standard) has a 90 nm outer diameter, and 20 nm thick Si wall. The equivalent Si nanorod (same amount of silicon) has an outer diameter of 74.8 nm. The *in situ* SEM observation Si nanotube has an 820 nm outer diameter, and a 75 nm thick Si wall.

nanotubes, the original total thickness is the thickness of the nanotube wall. Equations to convert thickness ratio to degree of lithiation are provided in the Supporting Information. Note, for the nanotubes, the degree of lithiation is equal to the thickness ratio, while for the nanorods, the degree of lithiation grows more rapidly than the thickness ratio. The detailed distributions of the maximum principal stresses and von Mises stresses in nanotubes and nanorods are given in Figure S19. The results show that, due to the elastic-perfectly plastic property of lithiated Si, the highest von Mises stress levels in lithiated regions of both nanotubes and nanorods are limited by the yield strength of 0.5 GPa. Furthermore, in both the nanotubes and the nanorods, the highest maximum principal stresses in lithiated regions are well below the tensile strength of lithiated Si, and that in the unlithiated Si (around 5 GPa) is also below the tensile strength of Si.[49] This is consistent with experimental observations that no cracks were present upon the first lithiation cycle. The lithiation-induced stress change in the Si nanorods is also in agreement with the report by Zhang *et al.*[23]

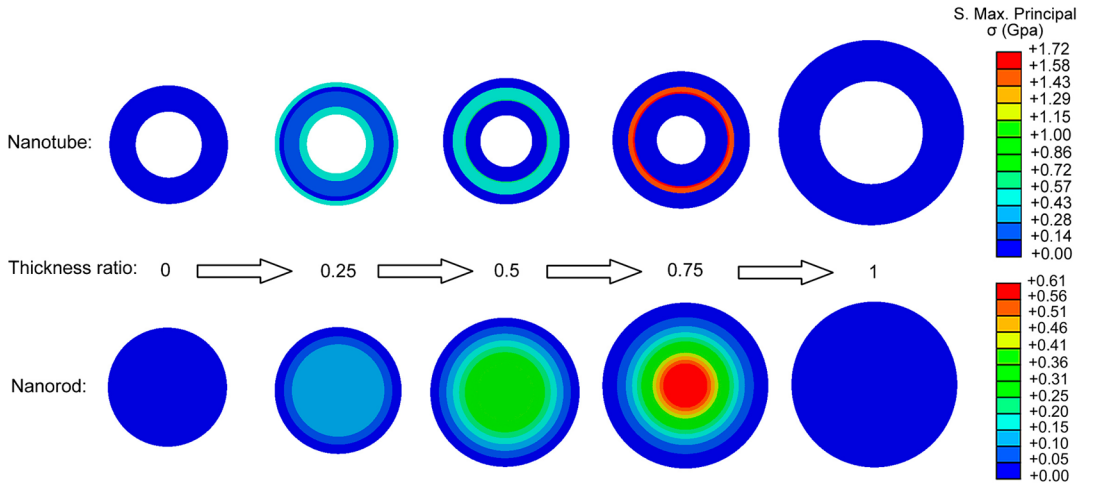

Figure 7. Maximum principal stress contours on deformed shapes of nanotubes and nanorods during lithiation as a function of the thickness ratio.

They stimulated the morphological changes and stress evolution of Si nanowires based on a finite-strain model, and showed that the predicted morphological change of the cross section of Si nanowires is similar to those by a small-strain model and some experimental reports.[50,51]

The situation is different if one considers the plastic strain in the nanotubes and nanorods. The highest plastic strain in the Si nanotubes and nanorods are plotted as a function of the thickness ratio in Figure 8. Although the highest plastic strains in nanotubes and nanorods are similar at the beginning of lithiation (low values of thickness ratio), they become very different as lithiation progresses. While the plastic strain in the nanotubes increases gently, the plastic strain in the nanorods increases dramatically. As the thickness ratio approaches 1.0, both structures becomes fully lithiated and the stresses and elastic strains in the structure go to zero.[52,53] However, the plastic strains do not go to zero. This is because, as previously demonstrated,[45,54] a core–shell structure forms in Si nanowires during lithiation. At the core–shell interface, a large strain is produced by the abrupt change of Li concentration, which can only relax by plastic deformation of the lithiated silicon. Figure 8 also shows that the highest plastic strain in the larger nanotube in the *in situ* SEM study is slightly less than that in the standard Si nanotubes in the electrochemical study. Plastic strain contours of nanotubes and nanorods through lithiation process are given in Figure 9. Evolutions of the plastic strain contours on deformed shape during lithiation of the nanorods and nanotubes are shown in Movies S2 and S3, respectively.

The numerical simulation results in Figures 8 and 9 also point to the possibility of a failure mechanism of the lithiated Si during charge–discharge cycles, *i.e.*, low-cycle fatigue. Low-cycle fatigue is induced by repeated plastic deformation, with a total cycle to failure fewer than 10^3 (often of the order of tens of

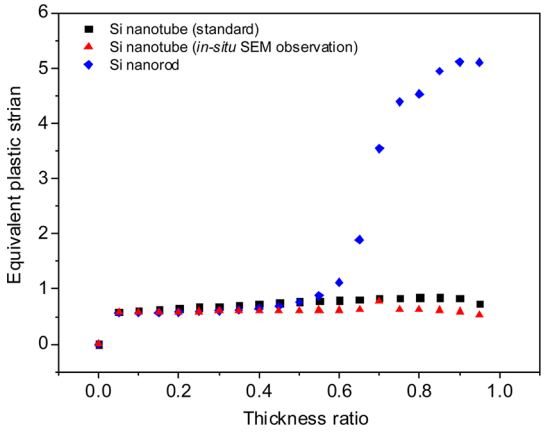

Figure 8. Maximum plastic strain in the silicon nanotubes and the nanorods as a function of lithiation (expressed as the thickness ratio as defined in the text).

cycles if large plastic deformation is present, *e.g.*, consider bending back and forth of a paper clip until failure). Low-cycle fatigue is governed by an empirical Coffin–Manson relation:[55]

$$\frac{\Delta\varepsilon_p}{2} = \varepsilon_f'(2N)^c \qquad (1)$$

where $(\Delta\varepsilon_p/2)$ is the plastic strain amplitude, ε_f' is the fatigue ductility coefficient, which is a constant, c is fatigue ductility exponent, which is a negative empirical constant, and N is the number of cycles to failure. As the material goes through the lithiation–delithiation cycles, significant plastic strain is accumulated, leading potentially to ratcheting phenomena. As a result, damage accumulates in the material which will eventually lead to failure. eq 1 shows that the higher the plastic strain amplitude, the lower the total number of cycle to failure. Since the plastic strain amplitude in the nanorods is significantly higher than that in the nanotubes, it is expected that the nanorods would fail with significantly fewer lithiation–delithiation cycles compared to the nanotubes. This is indeed observed in our

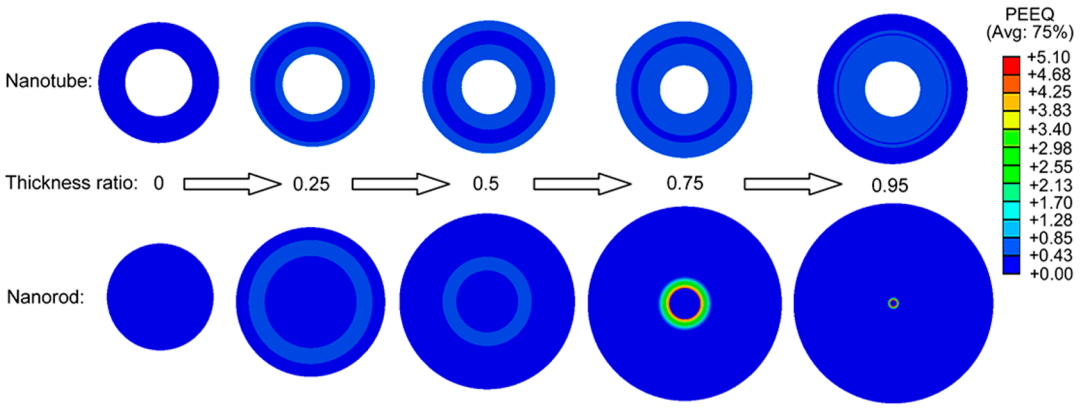

Figure 9. Plastic strain contours on deformed shapes of standard nanotubes and nanorods during lithiation as a function of thickness ratio. PEEQ stands for equivalent plastic strain.

experimental study, in which ZnO@C@Si@C nanorods with a solid ZnO core show obvious cracks after cycling (Figure S11e,f).

CONCLUSION

In summary, we have presented a sandwich structure design that effectively addresses the many of the mechanical and chemical stability issues common for Si anodes. The nanotube-based electrode exhibits a high volumetric capacity and stable Coulombic efficiency over cycling. *In situ* SEM cycling shows the tubes expand both inward and outward upon lithiation, as well as elongate, and then revert back to their initial size and shape after delithiation, suggesting a stable accommodation of volume changes. Stress modeling indicates the plastic strain during lithiation is much lower for the nanotube structure *vs* the nanorod structure, which is perhaps why the nanotube structures show much better cycling behaviors. In addition, the fact that the inner face of the nanotube showed minimal SEI formation is intriguing, and perhaps indicates the lithium is able to diffuse down the thin carbon layer during cycling. Clearly, additional studies are needed to investigate this further and to see if there is some optimal thickness of carbon and length of nanotube to realize the best cycling results. For example, perhaps the inner surface area of the tubes could be increased to provide both more sites for lithiation and to reduce the plastic strain. A few hexagram shaped inner-side nanotube models to investigate the shape-dependent plastic strain are shown in Figure S20. While these designs did not appear to offer significant advantages, we expect there may be optimal structures that have a far from round inner cross-section. It is also important to continue to investigate templates other than Ni foams, given the high density of Ni; however, it is important that any template be mechanically and chemically stable and have sufficient electrical conductivity.

METHODS

ZnO Nanorod Growth on Ni Foam. The ZnO nanorod array was prepared by a modified hydrothermal method.[56] Chemicals were purchased from Sigma–Aldrich Corp. and used directly without further purification. In a typical procedure, a 0.8 cm × 2 cm Ni foam (surface density: about 346 g m^{-2}, ~1 mm thick, 30–40 pores per centimeter, purity >99.99%, Marketech Intl, Inc.) was washed with acetone and water alternatively by ultrasonication and dried in a vacuum oven at 50 °C for 2 h. The pretreated Ni foam was dipped into 5 mM zinc acetate dehydrate solution for 1 min, followed by drying with a stream of N_2. This coating step was repeated twice. Then, the Ni foam was heated to 350 °C in air for 20 min, yielding a ZnO seed layer. The ZnO nanorod array was grown by immersing the seeded Ni foam into an aqueous solution containing 25 mM zinc nitrate-hydrate [$Zn(NO_3)_2 \cdot 6H_2O$] and 25 mM hexamethylenetetramine ($C_6H_{12}N_4$) at 93 °C for 4 h. After the reaction was complete, the Ni foam coated with ZnO nanorods was thoroughly rinsed with deionized water and ethanol, followed by drying in a vacuum oven at 50 °C for 3 h. For large tube fabrication for *in situ* SEM observation, large ZnO nanorods were prepared by three subsequent ZnO growths using fresh growth solution each time.

Carbon Coating on ZnO Nanorods. Furfuryl alcohol was employed as a carbon source similar to previous reports.[57] Typically, a Ni foam coated with ZnO nanorods was rapidly dipped into furfuryl alcohol. The wet foam was then heated in air at 150 °C for 24 h to polymerize the furfuryl alcohol. Afterward, carbonization was performed at 500 °C for 3 h under high purity Ar. A second coating on the ZnO@C@Si nanorods was conducted for the sandwich-structured C@Si@C nanotubes.

Si CVD. Si was deposited by static CVD system using disilane (Si_2H_6) as the Si source. The system was first evacuated to 10^{-6} mBar, followed by an introduction of 50 mbar of Si_2H_6 into the reaction chamber containing the desired sample. The chamber was sealed tightly and heated to 350 °C for 3 h. The ramp rate was 8 °C min^{-1}.

ZnO Core Etching. To etch ZnO nanorods to form the hollow nanotubes, 0.5 M acetic acid (aq) (HAc) was employed. HAc etches the ZnO nanorods, but not the Ni foam. For etching, samples were immersed into 20 mL of the HAc solution at room template for 30 min, thoroughly washed with deionized water, and dried in a vacuum oven at 50 °C prior to further use.

Characterization. Samples were characterized using a Hitachi S-4800 SEM, a Hitachi S-4700 equipped with an Oxford INCA EDX analyzer, a Philips X'pert MRD XRD with Cu Kα radiation (1.5418 Å), and a JEOL 2010 LaB6 TEM operating at 200 kV. Elemental mappings were performed on the Hitachi S-4700 SEM. The XRD peaks were compared with the Joint Committee on Powder Diffraction Standards (JCPDS). FIB characterization was carried out using a Helios 600i.

Electrochemical Measurements. Electrochemical tests were performed using two-electrode cells with lithium metal as the counter and reference electrode using Princeton Applied Research Model 273A and Biologic VMP3 potentiostats. The electrodes were set as the working electrodes. Cell assembly was carried out in an Ar-filled glovebox. An electrolyte consisting of 1 M of $LiClO_4$ in a 1:1 mass ratio mixture of ethylene carbonate and dimethylene carbonate was used. Electrode capacities were measured by a galvanostatic charge/discharge method at a rate of 0.07 C over the potential range of 0.005 to 2.0 V. CV of the C@Si@C nanotube array was recorded over the potential range of 0.0 to 2.0 V at a scan rate of 0.1 mV s^{-1}. In C-rate measurements, the current densities were changed from 0.05 C to 0.1, 0.5, 1.2, 2, and back to 0.05 C. At each of the C-rate, the electrode was cycled 8 times.

***In Situ* SEM Observations of Lithiation−Delithiation.** The working electrode was fabricated by dispersing acetone suspended C@Si@C nanotubes on a 3 mm carbon-coated Cu grid and drying at 80 °C. A 3 mm diameter composite $LiFePO_4$/carbon black/binder (8:1:1 by mass) counter electrode was cast on an Al current collector. Ionic liquid (10 wt % LiTFSI in P_{13}TFSI) was used as the electrolyte and the electrodes were isolated by a separator (Celgard). *In situ* lithiation−delithiation observations were performed on an SEM (FEI DB235). Electrical contacts were made in the SEM using micromanipulators. The battery was cycled potentiostatically (SP200, Biologic Co.), and SEM images were acquired automatically every minute.

Conflict of Interest: The authors declare no competing financial interest.

Acknowledgment. We thank Dr. Jiung Cho, Junjie Wang, Jingu Kang, and Sean J. Kelly for experimental assistance, and Dr. Jinjin Li for helpful discussions on electron transfer principles. Sample fabrication and characterization were carried out in the Frederick Seitz Materials Research Laboratory at the University of Illinois at Urbana−Champaign. All authors except Prof. Xingjiu Huang and Prof. Jinhuai Liu acknowledge the support from the U.S. Department of Energy, Office of Science, Basic Energy Sciences, under Award # DE-FG02-07ER46471. Prof. Xingjiu Huang and Prof. Jinhuai Liu acknowledge support from the State Key Project of Fundamental Research for Nanoscience and Nanotechnology of China (2011CB933700).

Supporting Information Available: We provide additional information, figures, and movies on material characterizations, electrochemical measurements, and modeling contours. This material is available free of charge *via* the Internet at http://pubs.acs.org.

REFERENCES AND NOTES

1. Goodenough, J. B. Evolution of Strategies for Modern Rechargeable Batteries. *Acc. Chem. Res.* **2013**, *46*, 1053–1061.
2. Song, H. W.; Yang, G. Z.; Cui, H.; Wang, C. X. Electrodes Engineering of High Power, Long Life and Excellent Cycling Stability for Rechargeable Lithium Batteries. *Nano Energy* **2014**, *3*, 16–25.
3. Ruzmetov, D.; Oleshko, V. P.; Haney, P. M.; Lezec, H. J.; Karki, K.; Baloch, K. H.; Agrawal, A. K.; Davydov, A. V.; Krylyuk, S.; Liu, Y.; *et al.* A. Electrolyte Stability Determines Scaling Limits for Solid-State 3D Li Ion Batteries. *Nano Lett.* **2012**, *12*, 505–511.
4. Barpanda, P.; Ati1, M.; Melot, B. C.; Rousse, G.; Chotard, J. N.; Doublet, M. L.; Sougrati, M. T.; Corr, S. A.; Jumas, J. C.; Tarascon, J. M. A 3.90 V Iron-Based Fluorosulphate Material for Lithium-Ion Batteries Crystallizing in the Triplite Structure. *Nat. Mater.* **2011**, *10*, 772–779.
5. Wang, F.; Yu, H. C.; Chen, M. H.; Wu, L. J.; Pereira, N.; Thornton, K.; Van-Der, A.; Zhu, Y. M.; Amatucci, G. G.; Graetz, J. Tracking Lithium Transport and Electrochemical Reactions in Nanoparticles. *Nat. Commun.* **2012**, *3*, 1201.
6. Zheng, G. Y.; Lee, S. W.; Zheng, L.; Lee, H. W.; Yan, K.; Yao, H. B.; Wang, H. T.; Li, W. Y.; Chu, S.; Cui, Y. Interconnected Hollow Carbon Nanospheres for Stable Lithium Metal Anodes. *Nat. Nanotechnol.* **2014**, *9*, 618–623.
7. Sun, J.; Zheng, G. Y.; Lee, H. W.; Liu, N.; Wang, H. T.; Yao, H. B.; Yang, W. S.; Cui, Y. Formation of Stable Phosphorus-Carbon Bond for Enhanced Performance in Black Phosphorus Nanoparticles-Graphite Composite Battery Anodes. *Nano Lett.* **2014**, *14*, 4573–4580.
8. Xu, Y. X.; Lin, Z. Y.; Zhong, X.; Huang, X. Q.; Weiss, N. O.; Huang, Y.; Duan, X. F. Holey Graphene Frameworks for Highly Efficient Capacitive Energy Storage. *Nat. Commun.* **2014**, *5*, 4554.
9. Xu, C. H.; Xu, B. H.; Gu, Y.; Xiong, Z. G.; Sun, J.; Zhao, X. S. Graphene-Based Electrodes for Electrochemical Energy Storage. *Energy Environ. Sci.* **2013**, *6*, 1388–1414.
10. Kim, G.; Jeong, S.; Shin, J. H.; Cho, J.; Lee, H. 3D Amorphous Silicon on Nanopillar Copper Electrodes as Anodes for High-Rate Lithium-Ion Batteries. *ACS Nano* **2014**, *8*, 1907–1912.
11. Yang, Y.; Zhang, H. L.; Liu, Y.; Lin, Z. H.; Lee, S.; Lin, Z. Y.; Wong, C. P.; Wang, Z. L. Silicon-Based Hybrid Energy Cell for Self-Powered Electrode Gradation and Personal Electronics. *ACS Nano* **2013**, *7*, 2808–2813.
12. Wu, H.; Chan, G.; Choi, J. W.; Ryu, I.; Yao, Y.; McDowell, M. T.; Lee, S. W.; Jackson, A.; Yang, Y.; Hu, L. B.; *et al.* Stable Cycling of Double-Walled Silicon Nanotube Battery Anodes Through Solid-Electrolyte Interphase Control. *Nat. Nanotechnol.* **2012**, *7*, 310–315.
13. Wu, H.; Cui, Y. Designing Nanostructured Si Anodes for High Energy Lithium Ion Batteries. *Nano Today* **2012**, *7*, 414–429.
14. McDowell, M. T.; Lee, S. W.; Nix, W. D.; Cui, Y. 25th Anniversary Article: Understanding the Lithiation of Silicon and Other Alloying Anodes for Lithium-Ion Batteries. *Adv. Mater.* **2013**, *25*, 4966–4985.
15. Philippe, B.; Dedryvere, R.; Gorgoi, M.; Rensmo, Hakan.; Gonbeau, D.; Edstrom, K. Role of the $LiPF_6$ Salt for the Long-Term Stability of Silicon Electrodes in Li-Ion Batteries—A Photoelectron Spectroscopy Study. *Chem. Mater.* **2013**, *25*, 394–404.
16. Wu, H.; Yu, G. H.; Pan, L. J.; Liu, N.; McDowell, M. T.; Bao, Z. N.; Cui, Y. Stable Li-Ion Battery Anodes by *In-Situ* Polymerization of Conducting Hydrogel to Conformally Coat Silicon Nanoparticles. *Nat. Commun.* **2013**, *4*, 1943.
17. Yi, R.; Dai, F.; Gordin, M. L.; Sohn, H.; Wang, D. H. Influence of Silicon Nanoscale Building Blocks Size and Carbon Coating on the Performance of Micro-Sized Si-C Composite Li-Ion Anodes. *Adv. Energy Mater.* **2013**, *3*, 1507–1515.
18. Lee, W. J.; Hwang, T. H.; Hwang, J. O.; Kim, H. W.; Lim, J.; Jeong, H. Y.; Shim, J.; Han, T. H.; Kim, J. Y.; Choi, J. W.; *et al.* N-Doped Graphitic Self-Encapsulation for High Performance Silicon Anodes in Lithium-Ion Batteries. *Energy Environ. Sci.* **2014**, *7*, 621–626.
19. Yu, B. C.; Hwa, Y.; Kim, J. H.; Sohn, H. Joon. Carbon Coating for Si Nanomaterials as High-Capacity Lithium Battery Electrodes. *Electrochem. Commun.* **2014**, *46*, 144–147.
20. Liang, B.; Liu, Y. P.; Xu, Y. H. Silicon-Based Materials as High Capacity Anodes for Next Generation Lithium Ion Batteries. *J. Power Sources* **2014**, *267*, 469–490.
21. Liu, N.; Lu, Z. D.; Zhao, J.; McDowell, M. T.; Lee, H. W.; Zhao, W. T.; Cui, Y. A Pomegranate-Inspired Nanoscale Design for Large-Volume-Change Lithium Battery Anodes. *Nat. Nanotechnol.* **2014**, *9*, 187–192.
22. Yang, H.; Huang, S.; Huang, X.; Fan, F. F.; Liang, W. T.; Liu, X. H.; Chen, L. Q.; Huang, J. Y.; Li, J.; Zhu, T.; *et al.* Orientation-Dependent Interfacial Mobility Governs the Anisotropic Swelling in Lithiated Silicon Nanowires. *Nano Lett.* **2012**, *12*, 1953–1958.
23. Yang, H.; Fan, F. F.; Liang, W. T.; Guo, X.; Zhu, T.; Zhang, S. L. A Chemo-Mechanical Model of Lithiation in Silicon. *J. Mech. Phys. Solids* **2014**, *70*, 349–361.
24. Applestone, D.; Yoon, S.; Manthiram, A. Mo_3Sb_7-C Composite Anodes for Lithium-Ion Batteries. *J. Phys. Chem. C* **2011**, *115*, 18909–18915.
25. Bogart, T. D.; Oka, D.; Lu, X. T.; Gu, M.; Wang, C. M.; Korge, B. A. Lithium Ion Battery Performance of Silicon Nanowires with Carbon Skin. *ACS Nano* **2014**, *8*, 915–922.
26. Hu, L. B.; Liu, N.; Eskilsson, M.; Zheng, G. Y.; McDonough, J.; Agberg, L. W.; Cui, Y. Silicon-Conductive Nanopaper for Li-Ion Batteries. *Nano Energy* **2013**, *2*, 138–145.

27. Wu, M. Y.; Sabisch, J. E. C.; Song, X. Y.; Minor, A. M.; Battaglia, V. S.; Liu, G. *In Situ* Formed Si Nanoparticle Network with Micron-Sized Si Particles for Lithium-Ion Battery Anodes. *Nano Lett.* **2013**, *13*, 5397–5402.
28. Wang, Y. H.; Liu, Y. P.; Zheng, J. Y.; Zheng, H.; Mei, Z. X.; Du, X. L.; Li, H. Electrochemical Performances and Volume Variation of Nano-Textured Silicon Thin Films as Anodes for Lithium-Ion Batteries. *Nanotechnology* **2013**, *24*, 424011.
29. Chan, C. K.; Peng, H. L.; Liu, G.; McIlwrath, K.; Zhang, X. F.; Huggins, R. A.; Cui, Y. High-Performance Lithium Battery Anodes Using Silicon Nanowires. *Nat. Nanotechnol.* **2008**, *3*, 31–35.
30. Wu, P.; Wang, H.; Tang, Y. W.; Zhou, Y. M.; Lu, T. H. Three-Dimensional Interconnected Network of Graphene-Wrapped Porous Silicon Spheres: *In Situ* Magnesiothermic-Reduction Synthesis and Enhanced Lithium-Storage Capabilities. *ACS Appl. Mater. Interfaces* **2014**, *6*, 3546–3552.
31. Jeong, G.; Kim, J. G.; Park, M. S.; Seo, M.; Hwang, S. M.; Kim, Y. U.; Kim, Y. J.; Kim, J. H.; Dou, S. X. Core-Shell Structured Silicon Nanoparticles@TiO_{2-x}/Carbon Mesoporous Microfiber Momposite as a Safe and High-Performance Lithium-Ion Battery Anode. *ACS Nano* **2014**, *8*, 2977–2985.
32. Ma, C. L.; Ma, C.; Wang, J. Z.; Wang, H. Q.; Shi, J. L.; Song, Y.; Guo, Q. G.; Liu, L. Exfoliated Graphite as a Flexible and Conductive Support for Si-Based Li-Ion Battery Anodes. *Carbon* **2014**, *7*, 238–246.
33. He, M. N.; Sa, Q. N.; Liu, G.; Wang, Y. Caramel Popcorn Shaped Silicon Particle with Carbon Coating as a High Performance Anode Material for Li-Ion Batteries. *ACS Appl. Mater. Interfaces* **2013**, *5*, 11152–11158.
34. Zhou, H.; Nanda, J.; Martha, S. K.; Unocic, R. R.; Meyer, H. M.; Sahoo, Y.; Miskiewicz, P.; Albrecht, T. F. Role of Surface Functionality in the Electrochemical Performance of Silicon Nanowire Anodes for Rechargeable Lithium Batteries. *ACS Appl. Mater. Interfaces* **2014**, *6*, 7607–7614.
35. Radvanyi, E.; Vito, E. D.; Porcher, W.; Danet, J.; Desbois, P.; Colin, J. F.; Larbi, S. J. S. Study of Lithiation Mechanisms in Silicon Electrodes by Auger Electron Spectroscopy. *J. Mater. Chem. A* **2013**, *1*, 4956–4965.
36. Chou, C. Y.; Hwang, G. S. Surface Effects on the Structure and Lithium Behavior in Lithiated Silicon: A First Principles Study. *Surf. Sci.* **2013**, *612*, 16–23.
37. Lotfabad, E. M.; Kalisvaart, P.; Kohandehghan, A.; Cui, K.; Kupsta, M.; Farbodab, B.; Mitlin, D. Si Nanotubes ALD Coated with TiO_2, TiN or Al_2O_3 as High Performance Lithium Ion Battery Anodes. *J. Mater. Chem. A* **2014**, *2*, 2504–2516.
38. Chen, Y.; Zeng, S.; Qian, J. F.; Wang, Y. D.; Cao, Y. L.; Yang, H. X.; Ai, X. P. Li^+-Conductive Polymer-Embedded Nano-Si Particles as Anode. Material for Advanced Li-Ion Batteries. *ACS Appl. Mater. Interfaces* **2014**, *6*, 3508–3512.
39. Chockla, A. M.; Harris, J. T.; Akhavan, V. A.; Bogart, T. D.; Holmberg, V. C.; Steinhagen, C.; Mullins, C. B.; Stevenson, K. J.; Korgel, B. A. Silicon Nanowire Fabric as a Lithium Ion Battery Electrode Material. *J. Am. Chem. Soc.* **2011**, *133*, 20914–20921.
40. Lee, D. C.; Hanrath, T.; Korgel, B. A. The Role of Precursor-Decomposition Kinetics in Silicon-Nanowire Synthesis in Organic Solvents. *Angew. Chem., Int. Ed.* **2005**, *44*, 3573–3577.
41. Xu, W.; Vegunta, S. S. S.; Flake, J. C. Surface-Modified Silicon Nanowire Anodes for Lithium-Ion Batteries. *J. Power Sources* **2011**, *196*, 8583–8589.
42. Janus, P.; Janus, R.; Kustrowski, P.; Jarczewski, S.; Wach, A.; Silvestre-Albero, A. M.; Rodríguez-Reinoso, F. Chemically Activated Poly(furfuryl alcohol)-Derived CMK-3 Carboncatalysts for the Oxidative Dehydrogenation of Ethylbenzene. *Catal. Today* **2014**, *235*, 201–209.
43. Zhao, K. J.; Pharr, M.; Vlassak, J. J.; Suo, Z. G. Fracture of Electrodes in Lithium-Ion Batteries Caused by Fast Charging. *J. Appl. Phys.* **2010**, *108*, 073517.
44. Wang, J. W.; He, Y.; Fan, F. F.; Liu, X. H.; Xia, S. M.; Liu, Y.; Harris, C. T.; Li, H.; Huang, J. Y.; Mao, S. X.; Zhu, T. Two-Phase Electrochemical Lithiation in Amorphous Silicon. *Nano Lett.* **2013**, *13*, 709–715.
45. Chon, M. J.; Sethuraman, V. A.; McCormick, A.; Srinivasan, V.; Guduru, P. R. Real-Time Measurement of Stress and Damage Evolution During Initial Lithiation of Crystalline Silicon. *Phys. Rev. Lett.* **2011**, *107*, 045503.
46. *ABAQUS*, Version 6.11, Abaqus Analysis User's Manual; Dassault Systemes: Providence, RI, 2011.
47. Chon, M. J.; Sethuraman, V. A.; McCormick, A.; Srinivasan, V.; Guduru, P. R. Real-Time Measurement of Stress and Damage Evolution During Initial Lithiation of Crystalline Silicon. *Phys. Rev. Lett.* **2011**, *107*, 045503.
48. Liu, X. H.; Wang, J. W.; Huang, S.; Fan, F. F.; Huang, X.; Liu, Y.; Krylyuk, S.; Yoo, J.; Dayeh, S. A.; Davydov, A. V.; *et al. In Situ* Atomic-Scale Imaging of Electrochemical Lithiation in Silicon. *Nat. Nanotechnol.* **2012**, *7*, 749–756.
49. Petersen, K. E. Silicon as a Mechanical Material. *Proc. IEEE* **1982**, *70*, 420–457.
50. Lee, S. W.; Mc-Dowell, M. T.; Berla, L. A.; Nix, W. D.; Cui, Y. Fracture of Crystalline Silicon Nanopillars During Electrochemical Lithium Insertion. *Proc. Natl. Acad. Sci. U. S. A.* **2012**, *109*, 4080–4085.
51. Liang, W.; Yang, H.; Fan, F.; Liu, Y.; Liu, X. H.; Huang, J. Y.; Zhu, T.; Zhang, S. Tough Germanium Nanoparticles Under Electrochemical Cycling. *ACS Nano* **2013**, *7*, 3427–3433.
52. Liu, X. H.; Zhong, L.; Huang, S.; Mao, S. X.; Zhu, T.; Huang, J. Y. Size-Dependent Fracture of Silicon Nanoparticles During Lithiation. *ACS Nano* **2012**, *6*, 1522–1531.
53. Goldman, J. L.; Long, B. R.; Gewirth, A. A.; Nuzzo, R. G. Strain Anisotropies and Self-limiting Capacities in Single-Crystalline 3D Silicon Microstructures: Models for High Energy Density Lithium-Ion Battery Anodes. *Adv. Funct. Mater.* **2011**, *21*, 2412–2422.
54. Liu, X. H.; Zheng, H.; Zhong, L.; Huang, S.; Karki, K.; Zhang, L. Q.; Liu, Y.; Kushima, A.; Liang, W. T.; Wang, J. W.; *et al.* Anisotropic Swelling and Fracture of Silicon Nanowires during Lithiation. *Nano Lett.* **2011**, *11*, 3312–3318.
55. Lefebvre, D.; Ellyin, F. Cyclic Response and Inelastic Strain Energy in Low Cycle Fatigue. *Int. J. Fatigue* **1984**, *6*, 9–15.
56. Baeten, L.; Conings, B.; Boyen, H. G.; D'Haen, J.; Hardy, A.; D'Olieslaeger, M.; Manca, J. V.; Van-Bael, M. K. Towards Efficient Hybrid Solar Cells Based on Fully Polymer Infiltrated ZnO Nanorod Arrays. *Adv. Mater.* **2011**, *23*, 2802–2805.
57. Nakamura, T.; Yamada, Y.; Yano, K. Monodispersed Nanoporous Starburst Carbon Spheres and Their Three-Dimensionally Ordered Arrays. *Microporous Mesoporous Mater.* **2009**, *117*, 478–485.